J. Fluid Mech. (2004), *vol.* 519, *pp.* 81–103.
DOI: 10.1017/S0022112004001302 Printed in the United Kingdom

Blade penetration into a vortex core with and without axial core flow

By X. LIU AND J. S. MARSHALL

Department of Mechanical and Industrial Engineering and IIHR – Hydroscience and Engineering, The University of Iowa, Iowa City, IA 52242, USA

(Received 31 October 2003 and in revised form 6 July 2004)

A computational study of the penetration of a blade into the core of an initially columnar vortex in an incompressible viscous fluid and the subsequent cutting of the vortex is reported for the case where the blade axis is initially orthogonal to the vortex axis. The vortex is advected toward the fixed blade by a free-stream velocity oriented tangent to the blade chord, where the free-stream speed is sufficiently large that the vortex does not induce ejection of vorticity from the blade boundary layer prior to impact of the vortex core with the blade leading edge. A range of computations are performed for cases both with and without ambient axial flow in the vortex core. As the blade leading edge penetrates into the vortex core, cross-diffusion between the columnar vortex and the blade boundary layer causes vortex lines originating in the columnar vortex to rapidly reconnect to those in the blade boundary layer. This cutting process is found to be always incomplete however, due to a change in sign of the spanwise vortex-induced velocity along the leading edge as the vortex is cut, leaving a thin vortex sheet that wraps around the blade leading edge. Cutting of a vortex with non-zero axial flow causes an asymmetry that results in an impulsive lift force on the blade. This lift force has maximum magnitude during the time period where the blade leading edge penetrates into the vortex core. Both the vortex cutting process and the unsteady lift force on the blade are found to be approximately independent of Reynolds number for the various cases examined.

1. Introduction

Orthogonal vortex–blade interaction occurs when a blade or airfoil passes through a columnar vortex structure such that both the blade spanwise direction and the direction of relative blade–vortex motion are orthogonal to the vortex axis. This type of vortex–blade interaction is commonly observed for helicopters in slow flight or hover conditions, in which the rotor wake vortices are advected down and impinge upon the helicopter tail rotor and tail section, leading to noise generation and impulsive moments on the vehicle (Leverton, Pollard & Wills 1977). A similar interaction occurs in pump intakes, where the intake vortex is repeatedly chopped by the pump impeller (Nagahara, Sato & Okamura 2001). Orthogonal vortex–blade interaction is commonly observed in a wide variety of propeller, fan and turbine situations due to ingestion of vortical structures into the rotor slipstream. One example of such an interaction occurs, for instance, when upstream boundary-layer turbulence is ingested into a ship or torpedo propeller, or when atmospheric turbulence is ingested into a helicopter rotor. In many such applications, the vortex exhibits a strong ambient axial core flow in addition to its circulatory motion. During orthogonal vortex–blade

interaction, the blade experiences a sudden force during its penetration into the vortex core, which can lead to degradation of rotor or propeller performance, material fatigue, and generation of undesirable noise.

Early experimental work on orthogonal vortex–blade interaction was conducted by Ahmadi (1986), Cary (1987), and Johnston & Sullivan (1992). These studies measured unsteady pressure on the blade surface and sound generation, and in some cases report flow visualization using smoke in a wind tunnel. The studies examine vortices generated by various means (usually from a rotating upstream blade) impacting on a fixed downstream body. While these studies give a first view of some of the complex physics associated with the vortex response to cutting by a blade, it is difficult to fully characterize the vortex–blade interaction from these results because the distinguishing features of the vortex flow immediately prior to cutting (e.g. strength, core radius, vorticity profile, axial velocity) are generally not known. The use of smoke for marking the flow in these experiments also yields limited information on vortex response as the blade impacts on the vortex core.

Other more recent experimental studies have focused on the vortex core response, including wave motion on the vortex core and ejection of boundary-layer vorticity from the blade. An experimental study of cutting of a vortex ring by a thin plate is reported by Weigand & Gharib (1997), who used particle-image velocimetry (PIV) to detect wave motion on the vortex core following cutting by the blade. An experimental study of the effect of vorticity ejected from the blade boundary layer on the vortex for cases with slow relative velocity between the vortex and blade (impact velocity) is reported by Krishnamoorthy & Marshall (1998), using a columnar intake vortex in water together with particle-image velocimetry (PIV) and laser-induced fluorescence (LIF) based diagnostics. For sufficiently slow blade motion, the vorticity ejected from the blade boundary layer wraps around the incident vortex, and can in some cases even disrupt the primary vortex, prior to vortex collision with the blade.

A computational and experimental study of the response of a vortex with non-zero axial flow following impulsive cutting by a thin blade is reported by Marshall & Krishnamoorthy (1997), where the computations are performed using an inviscid axisymmetric vortex method and the experiments are performed for a blade traversed through an intake vortex using LIF and PIV. Following cutting of a vortex with downward axial flow by a blade, the core radius of the vortex is observed to increase on the upstream (or 'compression') side and to decrease on the downstream (or 'expansion') side. For subcritical vortices, both an upstream-propagating 'compression wave' and a downstream-propagating 'expansion wave' are observed to form in the computations following cutting of the vortex by a thin blade. These waves consist of oscillating patterns of azimuthal vorticity, where far from the blade the compression wave has the form of a propagating vortex breakdown. In experiments with subcritical vortices, an upward-propagating bubble-type vortex breakdown is observed to occur immediately following cutting of the vortex by the blade. The computed vortex core area variation and the force on the blade for the subcritical case are found to compare well with the theoretical prediction of Marshall (1994). The speed of the upward-propagating vortex breakdown is also observed in both computations and experiments (Krishnamoorthy & Marshall 1994) to compare well with theoretical predictions for the 'vortex shock' speed. For supercritical vortices, only the expansion wave forms on the downstream side of the vortex. A similar increase in core radius on the upstream side of the vortex is evident in the computations presented by Lee, Burgraff & Lonlisk (1998) for a supercritical vortex.

The deformation of an inviscid vortex core due to penetration of a blade leading edge into the vortex core was examined computationally using a vortex method by Marshall & Grant (1996) for a case with no axial core flow. In an inviscid flow the vortex lines within the core bend around the blade leading edge and stretch, creating a region of strong vorticity just in front of the blade leading edge. During this penetration, the vortex induces a low-pressure region near the blade leading edge, which results in a force on the blade that draws it toward the vortex core. The computed value of the force on the blade for the inviscid theory is found to be similar to predictions using rapid distortion theory.

A series of wind-tunnel experiments examining orthogonal vortex–blade interaction have been reported by a group at Glasglow University (Green, Doolan & Cannon 2000; Wang *et al.* 2002). These experiments are notable in that not only is the blade pressure measured during cutting of the vortex, but the vortex characteristics (strength, core radius, axial flow, etc.) are measured as well. A study reporting data on vortex-induced blade forces and pressure fields during orthogonal vortex–blade interaction is reported by Wang *et al.* (2002). A study employing PIV to examine the vortex core response to cutting by a blade is given by Green *et al.* (2000). This study provides quantitative data on vortex core size change due to blockage of axial flow during vortex cutting. A study of the effect of cutting by multiple blades on the vortex-induced force is given by Doolan, Coton & Galbraith (2001). This study shows that prior cutting of a vortex by one blade can significantly reduce the force caused by cutting of the vortex by a second blade, which presumably occurs due to effects of reduction of the vortex axial flow caused by the first vortex cutting event.

The current study focuses on understanding the detailed fluid mechanics involved in cutting of a vortex by a blade, both with and without vortex axial flow. This problem involves cross-diffusion, and eventual vortex line reconnection, between the incident vortex and the blade boundary layer, which is accompanied by cutting off of the vortex axial flow at the blade location. The vortex cutting problem has not been examined in the previous computational literature, which used inviscid models and assumed instantaneous cutting of the vortex. Similarly, previous experimental studies have examined only the consequences of vortex cutting, such as transient blade lift force and wave propagation and core size variation of the vortex, rather than the fluid mechanics of the cutting process itself. This problem is of considerable importance because the blade lift force has its maximum magnitude as the blade leading edge penetrates into the vortex core, so studies assuming instantaneous vortex cutting would not be expected to capture this lift force accurately.

The present paper presents a computational study of the passage of a blade orthogonally through a columnar vortex in an incompressible viscous fluid. Due to computational limitations, the study is performed in a rather low Reynolds number range, with vortex Reynolds numbers $Re_V \equiv \Gamma/\nu = 44$–$488$ and blade Reynolds numbers $Re_B \equiv Uc/\nu = 300$–2000. The dominant physical processes governing the flow are primarily inviscid, although like other vortex reconnection problems, the presence of some slight viscosity is necessary in order for the vortex cutting (or reconnection) to occur. The computations are performed using a finite-volume method that is second-order accurate in both time and space on a block-structured grid (Lai 2000). A brief description of the computational model is given in § 2, along with results of a test of grid independence. Cases with a blade penetrating into a columnar vortex with no ambient axial flow are discussed in § 3. The effect of ambient axial flow in the vortex core on the vortex cutting process and unsteady blade force is examined in § 4. Conclusions are given in § 5.

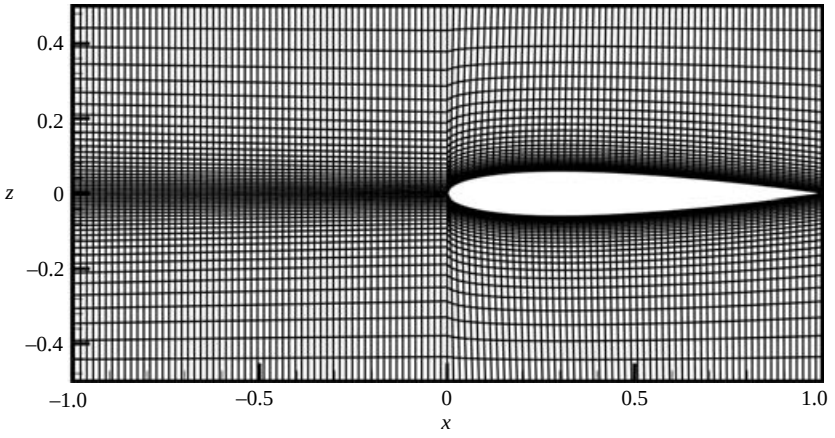

FIGURE 1. Cross-sectional view of the computational mesh.

2. Computational model

Computations are performed which solve the full Navier–Stokes equations in primitive-variable form using a finite-volume method (Lai 2000) and a block-structured mesh with hexahedral elements. The solution domain comprises 17 implicitly coupled blocks. As shown in the mesh cross-section in figure 1, the grid points are clustered to achieve high resolution within the vortex core, and particularly in the region where the vortex impacts upon the blade leading edge. The numerical method stores all dependent variables at the cell centres, and it uses a novel interpolation method to yield second-order-accurate approximation of the diffusive and convective fluxes on the cell boundaries for arbitrary meshes (even for unstructured meshes). The PISO algorithm (Issa 1985) is used to couple the momentum and continuity equations. In order to provide additional numerical stability, the time derivative is weighted between a second-order time derivative approximation and a first-order upwind approximation, with characteristically about 90–10 weighting ratio.

The computations are performed with a fixed blade subject to a uniform flow and a columnar vortex initialized upstream of the blade, as shown in figure 2. A Cartesian coordinate system is specified such that the uniform flow is in the x-direction, the blade span is in the y-direction, and the normal to the blade central plane is in the z-direction. Standard inflow and outflow boundary conditions are used in the x-direction, symmetry boundary conditions are used in the y-direction, and periodic boundary conditions are used in the z-direction. The computations are initialized by first performing a steady-flow computation with uniform speed U past a blade, shaped as a NACA0012 airfoil with maximum thickness T and chord length c. The flow domain is a box spanning the region $-3 \leqslant x/c \leqslant 1$, $-1.25 \leqslant y/c \leqslant 1.25$, and $-0.5 \leqslant z/c \leqslant 0.5$, where $z = 0$ coincides with the blade centreplane and the y-axis coincides with the blade leading edge. We then add to the steady flow velocity field a series of three columnar vortices with circulation Γ at a distance $d/c = 0.75$ upstream of the blade, where one vortex is within the computational domain and the other two vortices are in neighbouring periods of the computational domain. These vortices may either have zero axial flow or a prescribed non-zero axial flow according to the case under consideration. The initial axial vorticity and velocity fields have a Gaussian profile. An unsteady computation is then performed, during which time the vortex

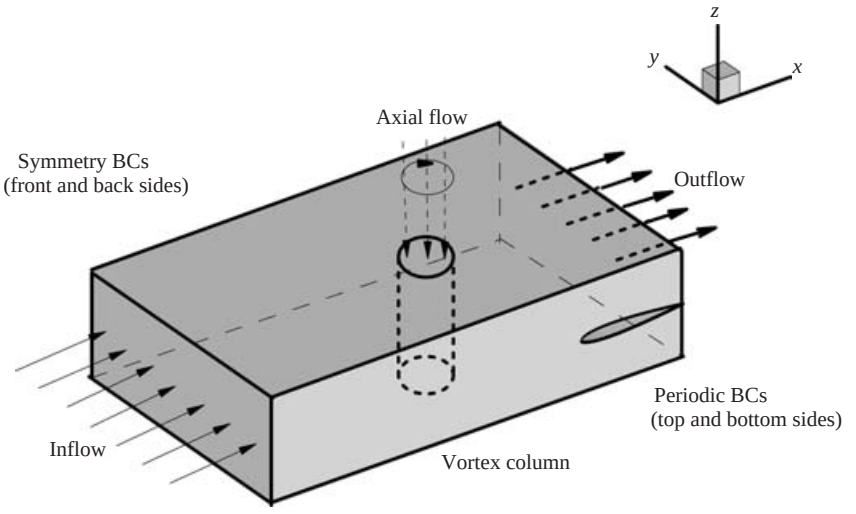

FIGURE 2. Schematic and boundary conditions for the computations.

is advected into the blade, and the computation stops when the vortex reaches the outlet end of the box. We let σ_0 and w_0 denote the core radius and maximum axial velocity obtained by fitting a Gaussian distribution to the vortex flow along the top boundary of the computational domain at a time $t = 0.75$ when the blade leading edge has penetrated to the nominal vortex centreline.

A variety of dimensionless parameters governing the orthogonal vortex–blade interaction problem can be defined in terms of these quantities. We define both a blade Reynolds number $Re_B \equiv Uc/\nu$ and a vortex Reynolds number $Re_V = \Gamma/\nu$, where ν is the kinematic viscosity. Dimensionless free-stream (impact) velocity U and vortex axial velocity w_0 can be divided by the nominal vortex maximum swirl velocity, $\Gamma/2\pi\sigma_0$, to form an 'impact parameter' $I \equiv 2\pi\sigma_0 U/\Gamma$ and an 'axial flow parameter' $A \equiv 2\pi\sigma_0 w_0/\Gamma$. An additional dimensionless parameter is formed by the ratio, T/σ_0, of the blade thickness T and the nominal vortex core radius σ_0. All variables in the remainder of the paper are non-dimensionalized using the blade chord length c as a length scale and the ratio c/U as a time scale.

The computations reported in the paper are selected in order to highlight the effect of these different dimensionless parameters on the transient blade lift force and to compare our viscous computational predictions with results of previous experimental and inviscid computational studies. A listing of the different computations performed is given in table 1. Set A includes cases with no axial flow within the vortex core. Case A.1 is used to compare with the predictions from the inviscid flow computations of Marshall & Grant (1996) for a blade penetrating into a vortex core. Cases A.2–A.4 are used to examine the effect of Reynolds number on orthogonal vortex–blade interaction. Set B includes cases with non-zero vortex axial flow. Case B.1 is for a subcritical axial flow, whereas Cases B.2–B.10 are for supercritical flow. Cases B.4–B.6 are the same as cases A.2–A.4 but with non-zero axial flow. Case B.3 is used to compare our computational results with the experimental data of Wang *et al.* (2002). Cases B.7–B.9 are used to evaluate the effect of impact parameter on the blade lift force, and Cases B.10 and B.4 are used to examine the effect of blade thickness on the lift force.

Case number	$2\pi\sigma_0 U/\Gamma$	T/σ_0	Re_V	$2\pi\sigma_0 w_0/\Gamma$	Re_B	Symbol (figure 22)
A.1	5.1	1.0	294	0	2000	
A.2	4.0	0.78	488	0	2000	O
A.3	4.0	0.78	244	0	1000	
A.4	4.0	0.78	73	0	300	
B.1	4.0	0.78	488	0.51	2000	+
B.2	10	0.56	45	0.85	1000	#
B.3	41	0.42	44	1.8	1000	*
B.4	4.0	0.78	488	3.8	2000	□
B.5	4.0	0.78	245	3.8	1000	Δ
B.6	4.0	0.78	73	3.8	300	∇
B.7	4.0	0.78	488	3.0	2000	◁
B.8	16	0.78	488	3.0	2000	▷
B.9	33	0.78	488	3.0	2000	◇
B.10	4.0	0.39	488	3.8	2000	%

TABLE 1. Summary of computations performed. Set A corresponds to zero axial flow and set B to non-zero axial flow.

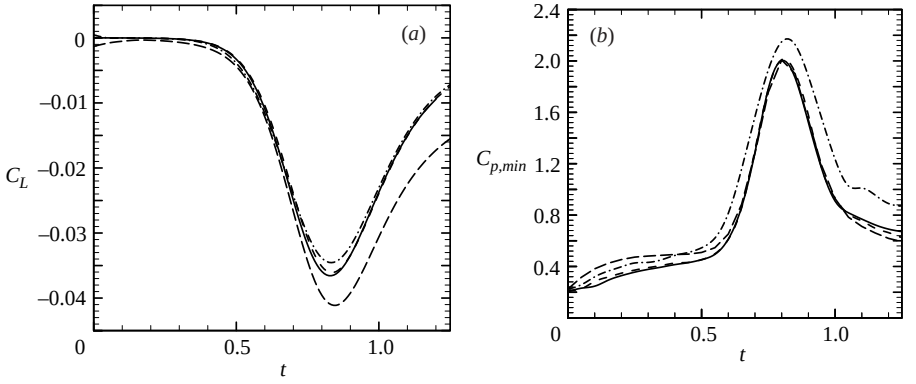

FIGURE 3. Time variation of (*a*) lift coefficient on the blade and (*b*) minimum surface pressure coefficient for 4 different meshes (Case B.4): mesh 1 (solid), mesh 2 (short-dashed), mesh 3 (dashed-dotted), and mesh 4 (long-dashed).

Grid independence is examined by repeating computations for Case B.4 for three different meshes, in which the number of computational points varies by a factor of 7.5 between the coarsest and finest mesh. The meshes are denoted by mesh 1 (994 000 grid points), mesh 2 (438 750 grid points), and mesh 3 (130 000 grid points). All computations are performed with a time step of 0.005, and all cover the same computational domain size. Over the time interval $0.5 \leqslant t \leqslant 1$, during which the blade cuts through the vortex core, the vortex circulation at the top surface of the flow domain decreases in mesh 1 and mesh 2 by 3.6% and in mesh 3 by 5.1%.

The time variation of the lift coefficient $C_L \equiv L/\frac{1}{2}\rho U^2 cb$, where b is the span length, L is the blade lift force, and ρ is fluid density, and the minimum blade surface pressure coefficient $C_{p,\min} \equiv (p_0 - p_{\min})/\frac{1}{2}\rho U^2$ are plotted for the three meshes in figure 3. Here p_0 denotes the pressure field on the blade surface in a steady flow with no vortex present. The blade first impacts on the outermost part of the vortex core at about time $t = 0.5$, and the blade has passed completely through the vortex core by about time $t = 1.0$. We observe that the computations converge as the mesh is refined, such that

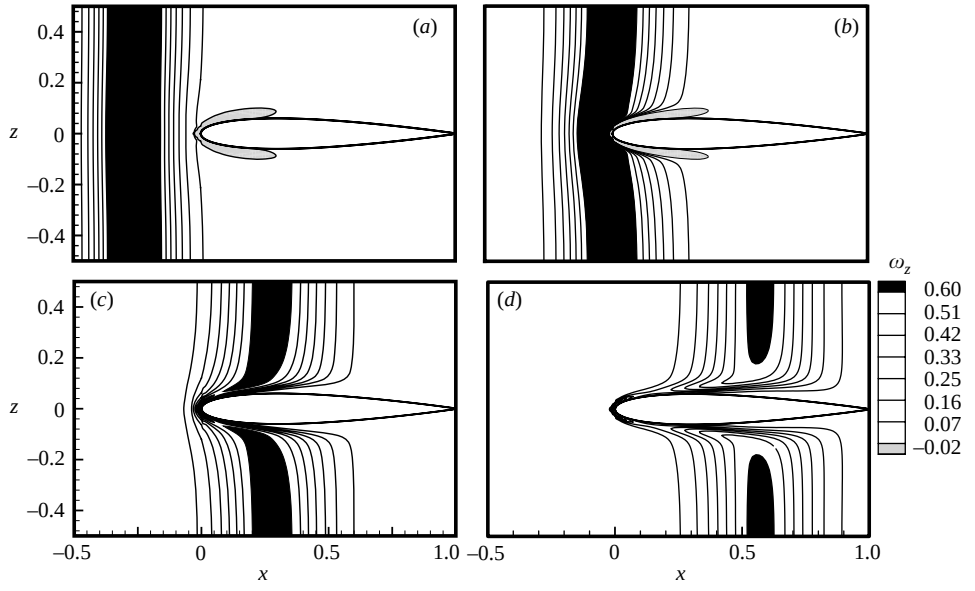

FIGURE 4. Contour plots of the z-component of vorticity at four different times during the vortex cutting process, for a case with no axial flow (Case A.2): (*a*) $t = 0.5$, (*b*) 0.75, (*c*) 1.0, (*d*) 1.25.

the computed values on the most refined mesh (mesh 1) differ from those in the medium refined mesh (mesh 2) by about by 1.4% for maximum lift magnitude and by 1.0% for the minimum pressure. The minimum pressure is particularly sensitive to spatial resolution because it is controlled by the thin vortex sheet wrapping around the blade leading edge (Marshall & Grant 1996). All of the subsequent computations reported are performed using the finest mesh (mesh 1).

The effect of height of the computational domain, in the direction of the vortex axis, is examined by repeating the computation with the same resolution as the medium mesh 2, but with twice the domain height, such that $-1 \leqslant z/c \leqslant 1$. The results for this computation are denoted by mesh 4 in figure 3(*a*, *b*). The predicted minimum pressure coefficient on the blade (figure 3*b*) for this case is very similar during the vortex cutting process to that for mesh 2. The maximum lift force coefficient (figure 3*a*) is nearly identical between mesh 2 and mesh 4 during the early part of the vortex cutting process. However, during the later part of the cutting process the computation with mesh 4 exhibits a larger peak in lift coefficient and a slower decay in lift force in comparison to the mesh 2 computation. The resulting maximum lift coefficient is about 13% larger for mesh 4 than it is for mesh 2. This effect would appear to be caused by the downstream wave propagation on the vortex core together with the presence of the periodic boundary condition in the z-direction. We have also compared qualitative aspects such as onset of boundary layer separation and contours of separated vorticity for mesh 2 and mesh 4 and found them to be nearly identical.

3. Case with zero ambient vortex axial flow

In this section we examine the basic physical processes occurring during penetration of a blade into a vortex core for cases with no ambient vortex axial flow. An illustration of this process is given in figure 4, in which contour lines of the vorticity component ω_z

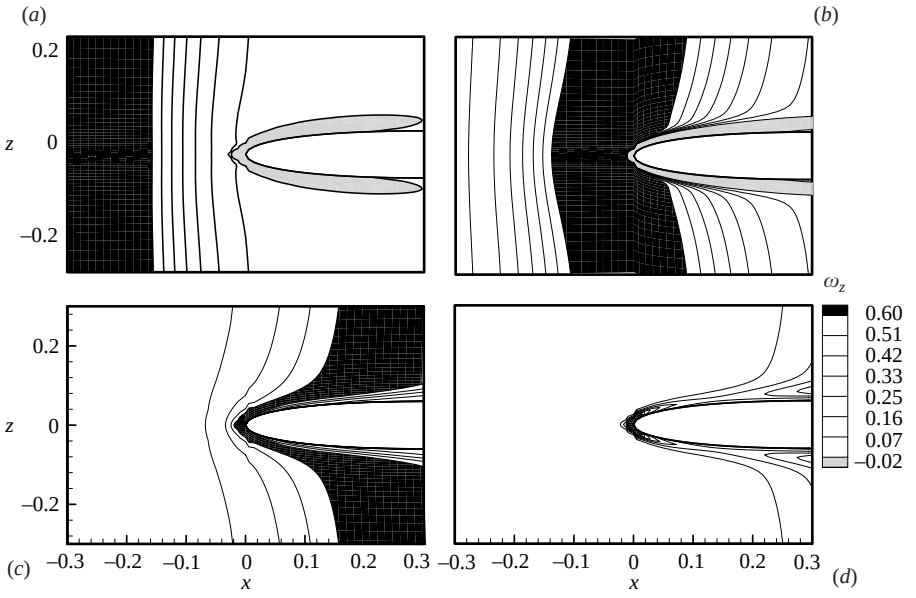

FIGURE 5. Close-up views of blade tip region for same four times shown in figure 4.

in the $y = 0$ plane for Case A.2 are plotted at four different times. Regions with highest values of ω_z are shaded black and those with lowest values of ω_z are shaded grey. At time $t = 0.5$, the blade is just penetrating the outer part of the vortex core, and there is little deformation of the vortex and no separation of the blade boundary layer. We observe a region with positive values of ω_z within the vortex core and a region with negative values of ω_z near the blade leading edge, which is caused by vorticity within the blade boundary layer that is generated by the spanwise vortex-induced flow. As the blade penetrates into the vortex core, the vortex core deflects around the blade leading edge and the vortex lines within the vortex core are stretched, leading to a region of increased values of positive ω_z within the part of the vortex core into which the blade penetrates (see figure 4*b* at $t = 0.75$). The blade penetration is accompanied by cross-diffusion of vorticity from the vortex and that within the blade boundary layer, resulting in rapid reconnection of vortex lines from the vortex to those in the blade boundary layer. However, once the blade has penetrated slightly over halfway through the vortex core, the sign of ω_z in the blade leading-edge boundary layer changes from negative to positive (see close-up views of the tip region in figure 5). This change in sign of ω_z is driven by a change in direction of the vortex-induced spanwise velocity component as the vortex centreline is swept past the blade leading edge. Following this change, the vorticity both within the blade boundary layer and within the vortex have positive values of ω_z, so the cross-diffusion between these two vorticity regions is eliminated and the vortex cutting is halted.

Another view of the same process is illustrated in figure 6, where we plot vortex lines in the $y = 0$ plane for the same four times as in figure 4. We initially observe deflection of vortex lines from the blade leading edge and rapid reconnection of vortex lines originating from the vortex to those in the blade boundary layer as the blade penetrates into the vortex core. However, after the blade has penetrated somewhat more than halfway through the vortex core, we observe that vortex lines stop reconnecting to those in the blade boundary layer, and instead continue to wrap

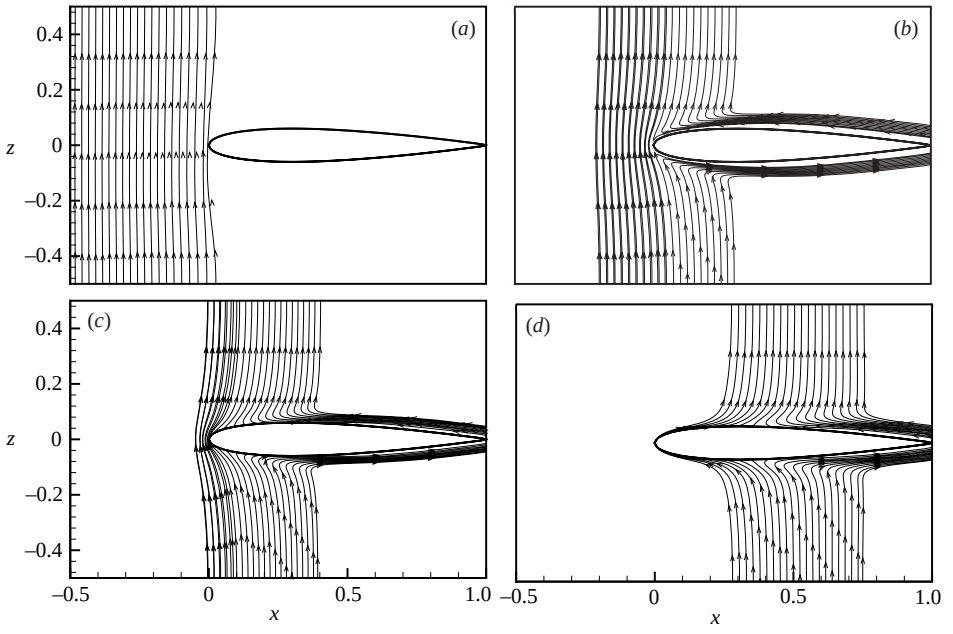

FIGURE 6. Vortex lines in the (x, z)-plane for the same four times shown in figure 4.

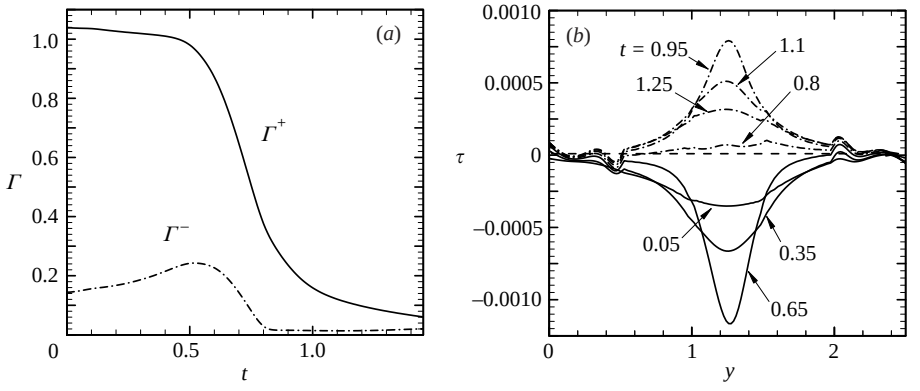

FIGURE 7. Results for Case A.2 showing (*a*) time variation of positive circulation (solid curve) and negative circulation (dashed-dotted curve) evaluated in the blade centreplane $z = 0$ and (*b*) time variation of the shear stress on the blade leading edge.

in a thin vortex sheet around the blade leading edge. This effect is particularly evident in figure 6(*d*), where we note that some vortex lines join to those in the boundary layer and deflect downstream, into the blade wake, while other vortex lines deflect upstream, wrap around the blade leading edge, and continue into the opposing section of the vortex.

A plot showing the time variation of the positive and negative circulation in the blade centreplane $z = 0$ is given in figure 7(*a*), which is obtained by separately integrating regions with positive and negative values of ω_z as follows:

$$\Gamma^+ = \int_A \omega_z^+ \, \mathrm{d}a, \quad \Gamma^- = \int_A \omega_z^- \, \mathrm{d}a, \tag{1}$$

where

$$\omega_z^+ = \begin{cases} \omega_z \text{ for all } z \text{ such that } \omega_z > 0 \\ 0 \text{ for all } z \text{ such that } \omega_z < 0, \end{cases}$$

$$\omega_z^- = \begin{cases} -\omega_z \text{ for all } z \text{ such that } \omega_z < 0 \\ 0 \text{ for all } z \text{ such that } \omega_z > 0. \end{cases}$$

Initially, Γ^+ is due to the columnar vortex and Γ^- is due to the blade boundary layer. In figure 7(*a*), the positive circulation is initially nearly constant and then decreases rapidly between times $t = 0.5$ and 1.0 as the blade penetrates into the vortex core. The negative circulation gradually increases as the vortex moves closer to the blade, reaches a peak after the blade has penetrated about one-quarter of the way through the vortex core, and then approaches zero after the blade has penetrated about two-thirds of the way through the vortex core. The rapid decrease of the negative circulation is associated with generation of positive ω_z within the part of the boundary layer near the blade leading edge, which occurs due to change in sign of the vortex-induced spanwise velocity as the vortex is advected past the leading edge. The reversal in direction of the spanwise velocity is evidenced by a change in sign of the shear stress along the blade leading edge at about $t = 0.8$, as shown in figure 7(*b*). This change in sign of ω_z halts the cross-cancellation of the blade boundary-layer vorticity with that within the columnar vortex. With no cross-diffusion, the remaining vortex lines are left to wrap around the blade leading edge and stretch as the vortex is advected forward. The stretching of these remaining vortex lines is balanced by viscous diffusion in a manner analogous to a Burgers vortex sheet. Although our computational domain was not sufficiently large to observe the long-time evolution of the system, we expect that the remaining vortex sheet wrapping about the blade leading edge will eventually decay in strength as the vortex advects sufficiently far downstream.

The formation of a remnant vortex sheet wrapping about the blade leading edge due to incomplete cutting of the columnar vortex has similarities to the formation of vorticity threads during reconnection of two vortex rings (see the review by Kida & Takaoka 1994), although the physics underlying the two phenomena are different. For vortex ring reconnection, the incomplete reconnection comes about because, as the percentage of vortex lines increases in the 'bridge' region spanning from one vortex ring to the other, the curvature of vortex lines in this region induces a velocity field that reverses the direction of the initial relative velocity between the two vortex rings, thus driving the two reconnecting vortices away from each other and leaving behind unconnected vorticity 'threads' (Melander & Hussain 1989). In the vortex cutting problem, it is the advection of the columnar vortex past the leading edge by the mean flow which causes this reversal of velocity resulting in incomplete reconnection of vortex lines with those in the blade boundary layer. Since the change in direction of the spanwise velocity at the leading edge is caused by inviscid advection of the vortex, we would not expect the percentage of uncut vortex to be sensitive to viscosity. To test this assumption, a series of Cases (A.2–A.4) have been run with different vortex Reynolds numbers (ranging from 73 to 488), but all other parameters the same. The variation of positive and negative circulation for these cases, plotted in figure 8, exhibits almost no change with Reynolds number. Plots showing vortex lines in the $y = 0$ plane with Reynolds numbers $Re_V = 73$ and 488 are given in figure 9. The lower Reynolds number case exhibits a substantially thicker blade boundary layer, as might be expected, but the vortex lines near the leading edge appear nearly the same in the two cases.

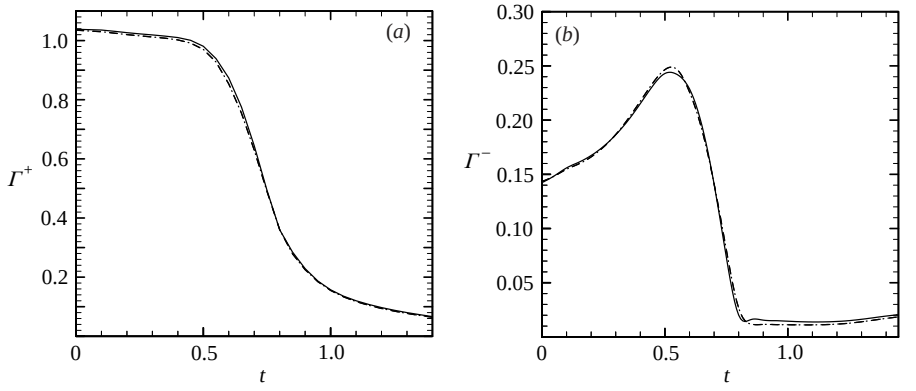

FIGURE 8. Effect of Reynolds number on the variation of (*a*) positive circulation and (*b*) negative circulation in the blade centreplane $z = 0$ for $Re_V = 488$ (Case A.2, solid curve), 244 (Case A.3, dashed curve), and 73 (Case A.4, dashed-dotted curve).

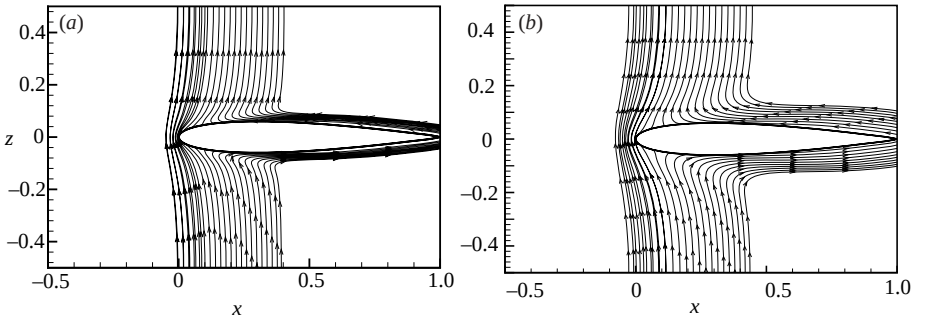

FIGURE 9. Vortex lines in the $y = 0$ plane for cases with (*a*) $Re_V = 488$ (Case A.2) and (*b*) $Re_V = 73$ (Case A.4).

As the vortex advects close to the blade, a region of low pressure forms along the blade leading edge. This low-pressure region is shown in figure 10(*a*), in which contour lines of the relative pressure coefficient $c_{p,rel}$ are plotted as a function of the arclength s of the blade cross-sectional profile and the spanwise distance y for the upper and lower surfaces of the blade at time $t = 0.8$ for Case A.2. The relative pressure coefficient is defined in terms of the difference between the pressure value $p(s, y, t)$ at the same point in the unsteady flow (with the vortex) and the pressure $p_{steady}(s, y)$ for the steady-state flow (without the vortex) as

$$c_{p,rel} = \frac{p(s, y, t) - p_{steady}(s, y)}{\frac{1}{2}\rho\, U^2}. \tag{2}$$

The time variation of the computed minimum pressure on the blade surface is compared with the inviscid flow computational results of Marshall & Grant (1996), obtained using a discrete vortex method, in figure 10(*b*) for Case A.1. In this figure we plot the vortex-based pressure coefficient $c_{p,V}$, defined by

$$c_{p,V} = \frac{p_{steady} - p_{min}(t)}{\rho\Gamma^2/2\sigma^2}, \tag{3}$$

where $p_{min}(t)$ is the minimum pressure on the blade surface at a given time. The time variation of the minimum pressure coefficient is observed to be in reasonable

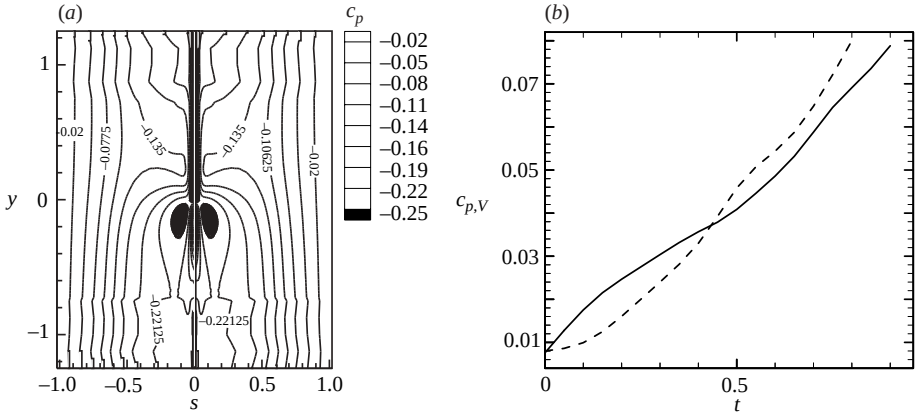

FIGURE 10. (*a*) Contours of pressure change coefficient $c_{p,rel}$ on the upper ($s < 0$) and lower ($s > 0$) sides of the blade surface at $t = 0.8$ (Case A.2), showing formation of low-pressure regions near the blade leading edge. (*b*) Time variation of vortex-based pressure coefficient $c_{p,V}$ at minimum pressure location on the blade surface for the current viscous flow computations (Case A.1, solid curve) and for the inviscid flow computations of Marshall & Grant (1996) (dashed curve).

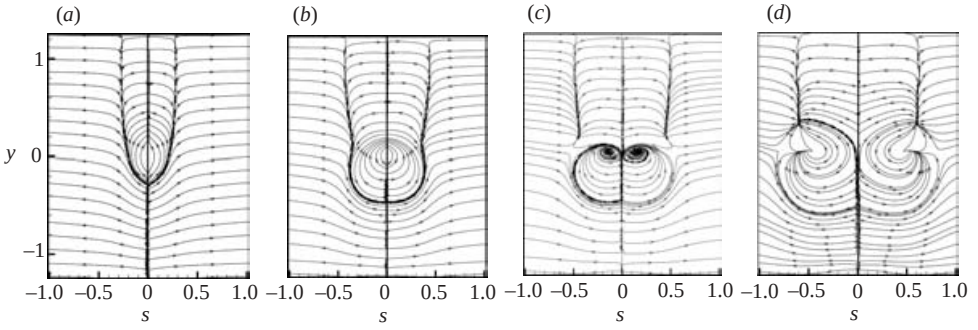

FIGURE 11. Limiting streamlines of the surface shear stress for the difference flow, obtained by subtracting the steady-state flow, for Case A.2 at times (*a*) $t = 0.5$, (*b*) 0.75, (*c*) 1.0, and (*d*) 1.25. The blade upper surface corresponds to $s < 0$ and the lower surface to $s > 0$.

agreement with inviscid results up to the time at which the blade has penetrated about three-quarters of the way through the vortex core, at which point the inviscid flow computations are discontinued. Beyond this point the viscous flow computations indicate that the minimum pressure coefficient peaks and then decreases.

Streamlines of the shear stress vector obtained from the perturbation velocity field are plotted on the blade surface at four different times for Case A.2 in figure 11. The steady-state velocity is subtracted from the full velocity field prior to plotting these streamlines in order to highlight the effect of the vortex-induced flow. The streamlines are useful in determining the direction of change, relative to the steady velocity field, caused by the presence of the vortex and the blade boundary layer response to the vortex. Before vortex impact on the blade (figure 11*a*), the vortex orientation is such as to increase the free-stream flow in the lower half of the figure and decrease the free-stream flow in the upper half of the figure. After the steady-state flow is subtracted, the latter region appears to be flowing toward the blade leading edge. A separatrix forms on the upper part of figure 11(*a*), on the side of the blade where the vortex-induced

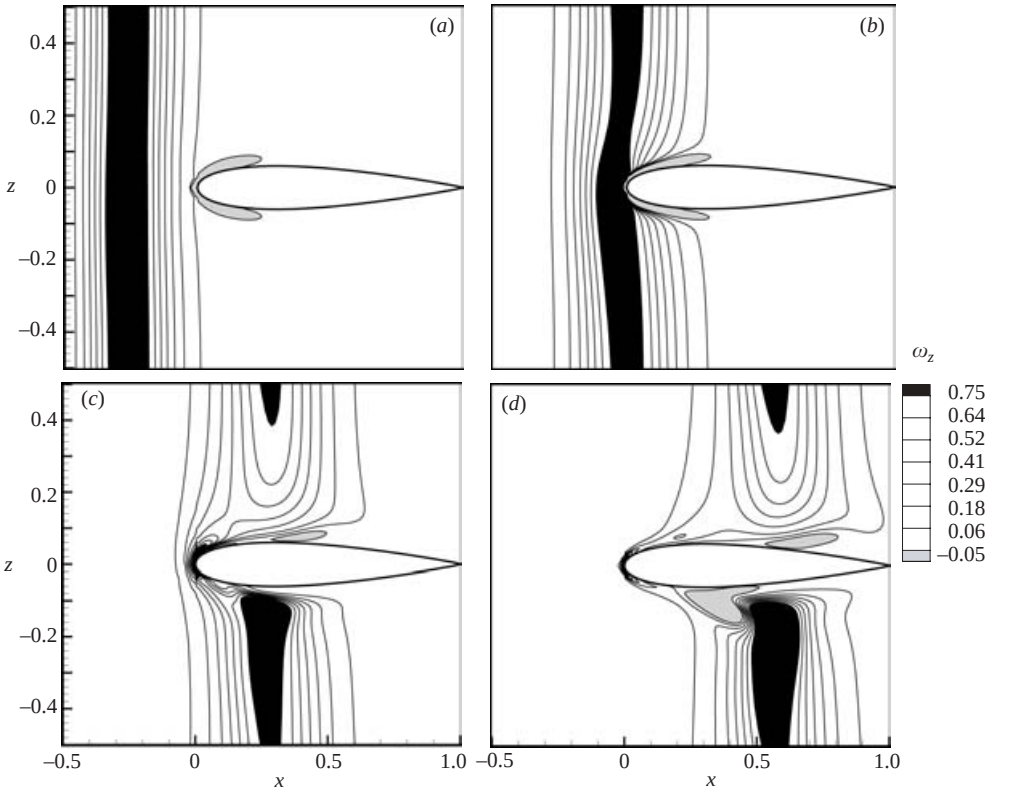

FIGURE 12. Contour plots of ω_z during the vortex cutting process for a case with supercritical vortex axial flow (Case B.4) at times (*a*) $t = 0.5$, (*b*) 0.75, (*c*) 1.0, and (*d*) 1.25.

flow is oriented opposite to the direction of the free-stream velocity. As the blade begins penetrating into the vortex core (figure 11*b*) the region in which the vortex-induced velocity perturbation is oriented in the upstream direction increases in size. As the vortex lines from the vortex begin to reattach to those in the blade boundary layer, inward-spiralling centre points form on each side of the blade, corresponding to the centre of the cut vortex (figure 11*c*). Once the cut vortex advects back onto the blade surface (figure 11*d*), we observe the formation of lines of flow convergence originating near the vortex centers and trailing downstream. Since these convergence lines are oriented in the streamwise direction, they would remain even after adding the steady-state flow back in. This suggests that the blade boundary layer separates along these convergence lines, feeding boundary-layer vorticity into the vortex core. Similar entrainment of blade boundary-layer vorticity following vortex cutting was observed experimentally by Krishnamoorthy & Marshall (1994) by injecting yellow dye along the blade leading edge and illuminating entrainment of the dye into the cut vortex core (dyed red) using laser-induced fluorescence.

4. Cases with axial core flow

Cases with various axial flow rates have been examined to determine the effect of vortex axial flow on the vortex-induced blade force and the vortex-cutting process. Plots showing contours of ω_z at different times for a case with supercritical vortex flow (Case B.4) are given in figure 12. In contrast to the case with no axial flow shown

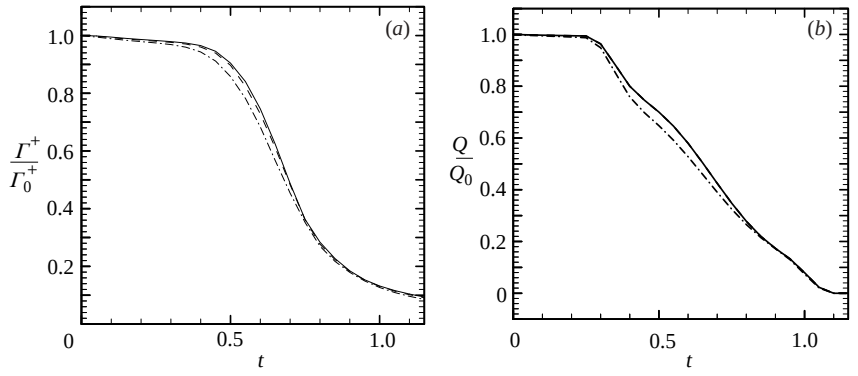

FIGURE 13. Effect of Reynolds number on (*a*) positive circulation and (*b*) flow rate in the z (axial) direction in the blade centreplane $z = 0$, non-dimensionalized by their initial values, plotted for Cases B.4 (solid curve), B.5 (dashed curve), and B.6 (dashed-dotted curve).

in figure 4, we observe an intensification of ω_z in the part of the vortex below the blade and a decrease in ω_z in the part of the vortex above the blade, corresponding to a decrease and increase in core radius, respectively. This phenomenon is due to the effect of the decrease in axial flow rate as the fluid approaches the blade from above in compressing vortex lines aligned in the z-direction, and the corresponding stretching of vortex lines below the blade as the axial flow accelerates to the ambient value. Similar variation in the vortex core radius is observed in the inviscid flow computations with instantaneous vortex cutting and in the LIF experiments by Marshall & Krishnamoorthy (1997), as well as in the PIV measurements of orthogonal vortex–blade interaction by Green *et al.* (2000).

Another difference that is apparent in comparing the results with axial flow in figure 12 for Case B.4 to those without axial flow in figure 4 for Case A.2 is the ejection of blade boundary-layer fluid from the lower blade surface following vortex cutting. This vorticity ejection can be observed in figure 12(*d*) as a finger of fluid emanating from the lower side of the blade boundary just upstream of the cut vortex. The ejection of blade boundary-layer fluid occurs at the location where the vortex-induced velocity opposes the free-stream velocity, leading to velocity back-flow within the boundary layer. This boundary-layer ejection does not occur immediately when the vortex is cut (e.g. in figure 12*c*), but forms later after stretching by the axial flow has sufficiently strengthened the vorticity in the lower portion of the vortex. The fact that similar boundary-layer ejection does not occur for the upper half of the vortex or for the case without axial flow is no doubt due to the fact that the vorticity within the vortex core is weaker in these cases, such that the vortex-induced velocity magnitude just outside the core is smaller.

Prior to performing the study, we had speculated that the vortex axial flow would cause separation from the blade leading edge as it penetrates into the vortex core. It is interesting that we do not observe separation from the leading edge in any of the computational cases considered in the current study. Rather, the reconnection of vortex lines from the vortex to those within the blade boundary layer, and the subsequent blockage of the axial flow, appears to occur quickly enough that separation from the leading edge does not have a chance to occur. To examine this point further, the time variation of the positive circulation Γ^+ and the axial flow rate $Q = \int_{-\infty}^{\infty}\int_{-\infty}^{\infty} w \, \mathrm{d}x \, \mathrm{d}y$ evaluated in the blade centreplane $z = 0$, non-dimensionalized by their initial values, are plotted in figure 13 for three different vortex Reynolds

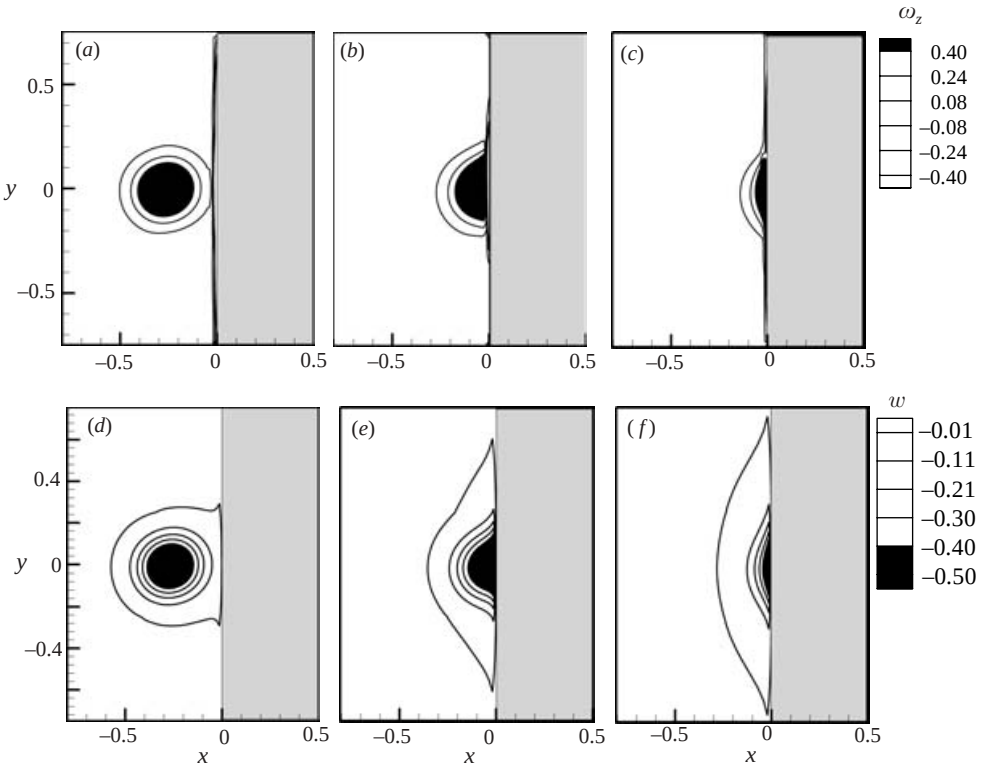

FIGURE 14. Time series showing contours of axial vorticity ω_z (*a–c*) and axial velocity w (*d–f*) and in the blade centreplane $z = 0$ for Case B.4 at times (*a*, *d*) $t = 0.5$, (*b*, *e*) 0.75, (*c*, *f*) 0.9.

numbers (Cases B.4–B.6). The positive circulation decreases abruptly at a time of about $t = 0.5$, as the blade leading edge penetrates into the vortex core. The rate of decrease of the positive circulation starts to level off at a time of about 0.8, just after the blade leading edge passes the nominal vortex centreline, and continues levelling off with increasing time. The axial flow rate begins decreasing much earlier than the positive circulation, at a time of about $t = 0.3$, due to the fact that the azimuthal vorticity responsible for the axial flow lies on the periphery of the vortex core rather than in the core centre. The axial flow rate decreases nearly linearly with time until it goes approximately to zero at a time of about $t = 1.1$, at which point the blade leading edge has passed entirely through the nominal vortex core position. Neither the positive circulation nor the axial flow rate exhibit significant dependence on Reynolds number.

Contour plots of axial vorticity ω_z and axial velocity w in the blade centreplane $z = 0$ are given for three different times during the blade penetration into the vortex core in figure 14. At time $t = 0.5$, we observe positive ω_z values within the vortex core and negative ω_z within the blade boundary layer. The vortex core shape is slightly elliptical in both the axial vorticity and axial velocity plots. At $t = 0.75$, the vortex core has become highly deformed and the region of negative vorticity within the blade boundary layer has diminished in size. At $t = 0.9$, at which point the blade leading edge has passed nearly completely through the vortex core, the vortex has deformed into a thin sheet along the leading edge with a bulge in the middle. The sign of

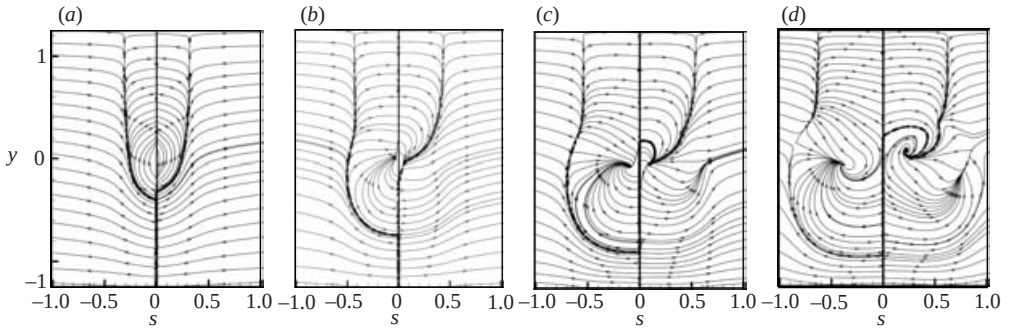

FIGURE 15. Limiting streamlines of the surface shear stress for the difference flow, obtained by subtracting the steady-state flow, for Case B.4 at times (*a*) $t = 0.5$, (*b*) 0.75, (*c*) 1.0, and (*d*) 1.25. The blade upper surface corresponds to $s < 0$ and the lower surface to $s > 0$.

vorticity within the blade boundary layer has changed to be the same as that within the vortex, as described in the previous section.

The breakdown of symmetry between the upper and lower sides of the blade due to the presence of vortex axial flow is also observed by comparing the streamlines of the shear stress of the perturbation velocity on the blade surface (obtained by subtracting the steady-state velocity from the full velocity field) for Case B.4 (figure 15) to that for Case A.2 without axial flow (figure 11). Prior to impact of the blade onto the vortex core, the shear streamlines of the perturbation velocity field appear almost symmetric (e.g. figure 15*a* at $t = 0.5$). However, almost immediately following impact of the blade leading edge on the outer surface of the vortex core (figure 15*b*) the streamlines become highly non-symmetric, with the separatrix growing larger on the upper surface of the blade and diminishing abruptly on the lower surface. As the vortex is cut and advects away from the leading edge, we observe inward-swirling streamlines, indicative of the presence of significant entrainment of boundary-layer fluid into the vortex core.

The asymmetry in flow field between the upper and lower sides of the blade leads to differences in blade surface pressure, which subsequently leads to a transient lift force on the blade. The pressure is initially nearly symmetric between the upper and lower surfaces when the vortex is located well upstream of the blade. The pressure asymmetry following vortex cutting is exhibited in figure 16, in which the difference between the blade surface pressure coefficient $c_p \equiv (p - p_0)/\frac{1}{2}\rho U^2$ for Case B.4 with axial flow and that for Case A.2 without axial flow is plotted at $t = 1.25$ as a function of the arclength s around the blade profile. Consistent with the observed variation in core radius, it is found that the pressure on the upper blade surface increases and that on the lower surface decreases compared to the case without axial flow. This difference gives rise to a net downward lift force on the blade.

The integral of the blade surface pressure times the surface unit normal over a cross-section L of the blade is used to form the normal force coefficient $C_N \equiv -\int_L p\boldsymbol{n}\,\mathrm{d}s$, which is of interest because it can be measured experimentally using an array of pressure transducers embedded in the blade surface. A plot of the time variation of the computed normal force coefficient for Case B.3 is compared in figure 17 with experimental results of Wang *et al.* (2002) for a comparable case with impact parameter $I = 36.8$, axial flow parameter $A = 1.62$, and ratio of blade thickness to vortex core radius $T/\sigma_0 = 0.42$. These parameters are within 10% of those given in table 1 for Case B.3. It is noted that some of the experimental vortex parameters (such

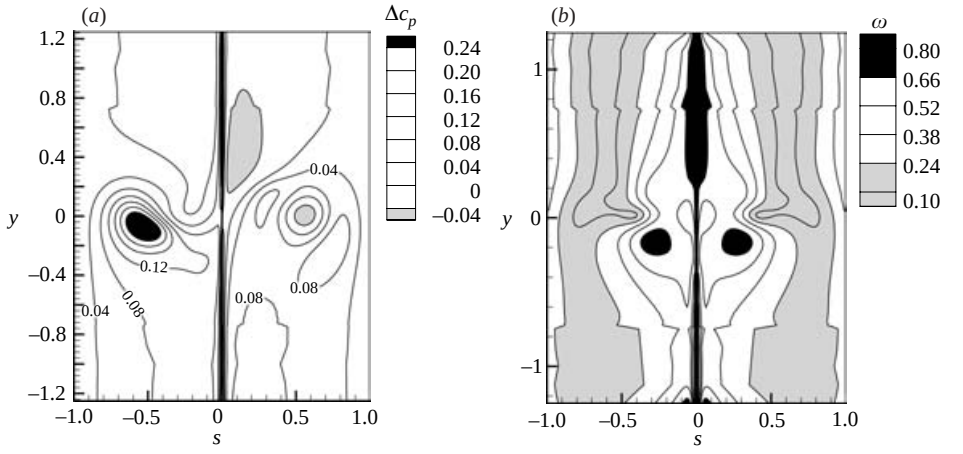

FIGURE 16. Results for variation of quantities on the blade surface at time $t = 1.25$ for (*a*) difference in surface pressure coefficient c_p between Case B.4 with axial flow and Case A.2 without axial flow and (*b*) contour plots of the magnitude of the surface tangential vorticity, after subtracting the steady-state flow, for Case A.2. The blade upper surface corresponds to $s < 0$ and the lower surface to $s > 0$.

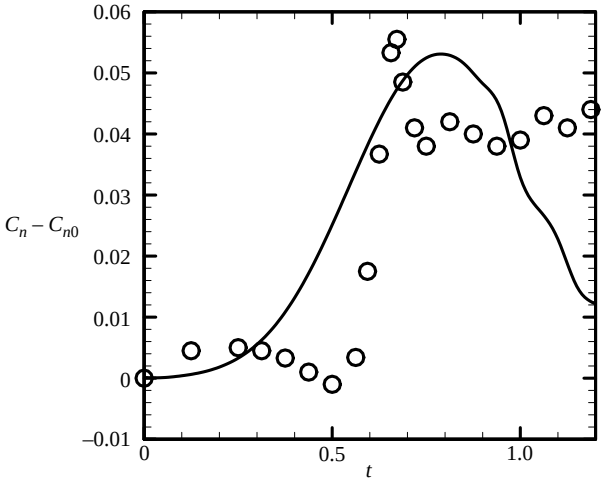

FIGURE 17. Comparison of the computed normal force coefficient within a slice at $y = 0$ for the current computations for Case B.3 (solid curve) and the experimental data of Wang *et al.* (2002) (circles).

as vortex circulation and core radius) have large experimental uncertainties due to the inherent difficulty in measuring the unsteady vortex state. For instance, Wang *et al.* (2002) report 35% uncertainty in vortex circulation and 55% uncertainty in vortex core radius. The experimental data for the normal force coefficient exhibit a rapid increase during penetration of the blade into the vortex core, followed by a levelling out to a constant value following cutting. The computational results yield a peak value of the normal force coefficient that is close to that in the experimental data, but the computations exhibit a slower increase in blade normal force during the initial stages of blade penetration into the vortex core and the computed normal force coefficient decreases following cutting of the vortex, rather than maintaining a nearly constant

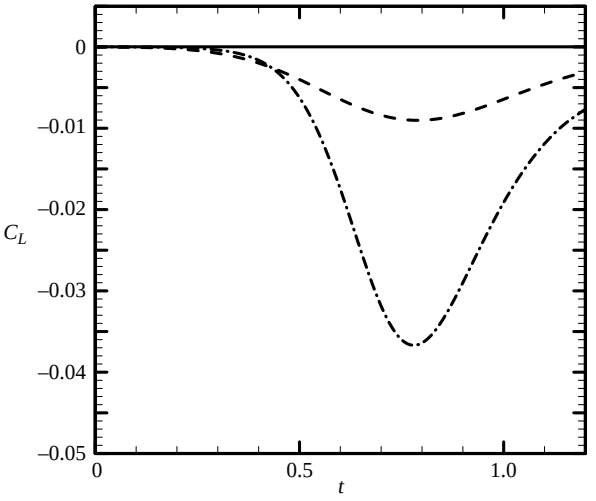

FIGURE 18. Effect of vortex axial flow parameter on the lift coefficient on the blade, for Case A.2 ($A = 0$, solid curve), Case B.1 ($A = 0.51$, dashed curve) and Case B.4 ($A = 3.8$, dashed-dotted curve).

value as seen in the experiments. These differences between the experimental and computational results are most likely due to the large difference in vortex Reynolds number in the two cases, which measured about $Re_V = 51\,000$ in the experiments and about $Re_V = 44$ in the computations in Case B.3. The vortex would be expected to exhibit more deformation of the vortex lines during penetration as the Reynolds number increases because the vorticity cross-diffusion rate between the vortex core and the blade leading-edge boundary layer would be slower at higher Reynolds numbers for a given vorticity gradient. As the blade penetrates further into the vortex core (and the vortex lines deform around the blade leading edge), the vorticity gradient at the leading edge increases, allowing the vorticity cross-diffusion rate to approach the values that it would have for a more viscous fluid at a time with less blade penetration. Delay of the vortex reconnection at higher Reynolds number would cause the vortex to stretch into a thin sheet wrapped around the blade leading edge at the penetration location (as observed in the inviscid computations at Marshall & Grant 1996), so that cutting of the axial flow (and subsequent imposition of the lift force on the blade) would occur over a shorter time period for a high Reynolds number case than for a lower Reynolds number case. Viscous decay of the vortex would also explain the observed decrease in normal force coefficient near the end of the computations.

The effect of axial flow parameter on the blade lift coefficient, generated by asymmetry in the pressure field, is plotted in figure 18 for Case A.2 (with no axial flow), Case B.1 (subcritical axial flow, $A = 0.51$) and Case B.4 (supercritical axial flow, $A = 3.8$). The magnitude of the lift force increases with time from nearly zero for times before the blade penetrates into the vortex core ($t < 0.5$), peaks at a time at which the blade leading edge has penetrated just past the vortex centroid ($t \approx 0.84$), and then decays gradually with later time. Significant lift force exists even after the vortex has been cut by the blade ($t > 1$) due to the asymmetry between the upper and lower blade surfaces. The maximum lift magnitude is zero for the case with no axial flow and increases monotonically as the axial flow rate is increased.

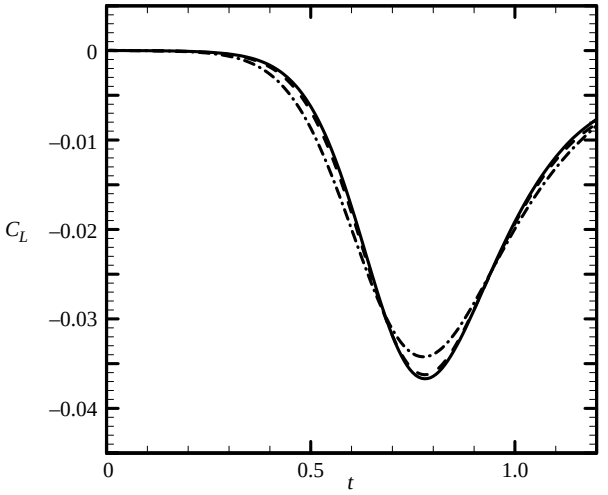

FIGURE 19. Effect of vortex Reynolds number on time variation of blade lift force, plotted for Cases B.4 (solid curve), B.5 (dashed curve), and B.6 (dashed-dotted curve).

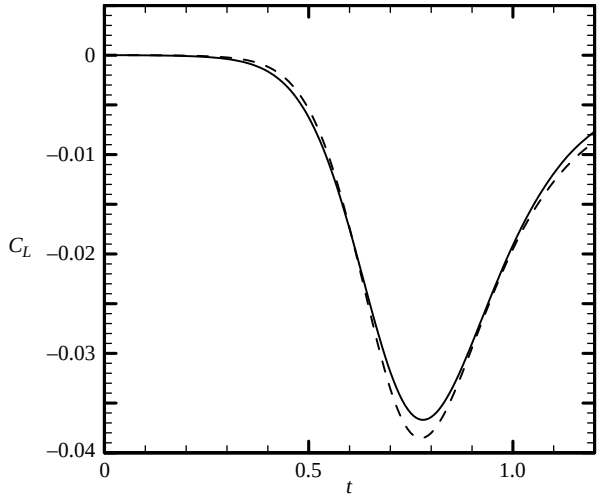

FIGURE 20. Effect of blade thickness on pressure-induced lift coefficient on the blade, for Case B.4 ($T/\sigma_0 = 0.78$, dashed curve) and Case B.10 ($T/\sigma_0 = 0.39$, solid curve).

The blade lift coefficient is plotted for three different vortex Reynolds numbers in figure 19, with the same values of axial flow parameter and impact parameter (Cases B.4–B.6). Within the range of variation considered in this work, the Reynolds number appears to have relatively little effect on the lift force. For instance, as the vortex Reynolds number increases by a factor of 6.7, the maximum lift force in figure 19 changes only by about 8%. Similarly, figure 20 shows lift coefficient for two cases with different blade thickness (Case B.4 with $T/\sigma_0 = 0.78$ and Case B.10 with $T/\sigma_0 = 0.39$), but all other variables held the same. The maximum lift force differs by only about 5% for these two cases.

The effect of impact parameter on lift force is examined in figure 21, where we plot lift force coefficient for cases with three different values of the free-stream velocity

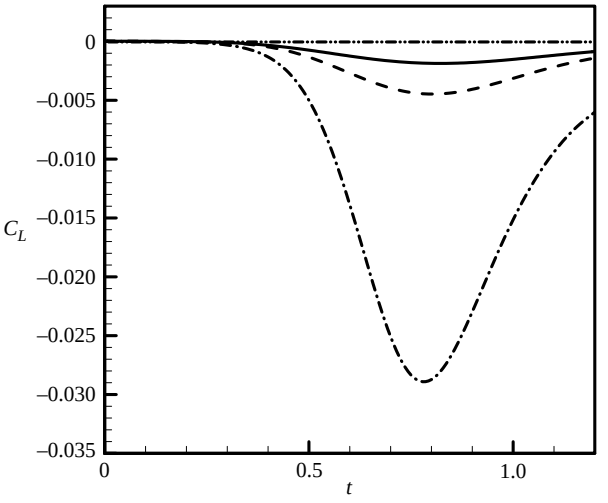

FIGURE 21. Effect of impact parameter on time variation of blade lift force plotted for Cases B.7 (dashed-dotted curve), B.8 (dashed curve), and B.9 (solid curve).

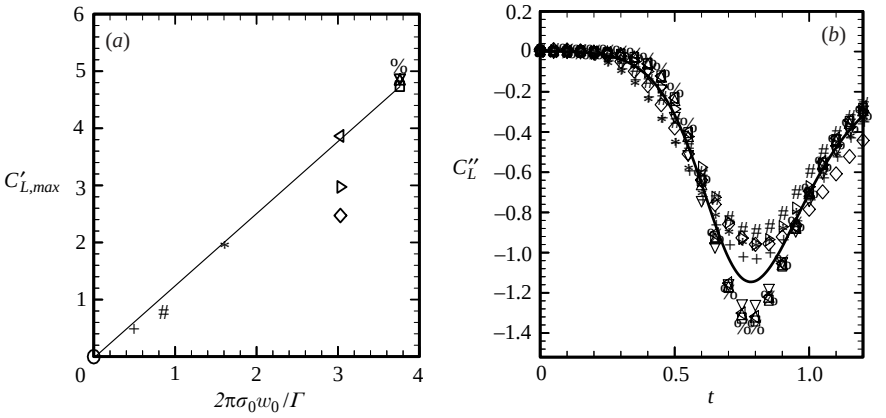

FIGURE 22. Correlations for lift force coefficients using data from Cases B.1–B.10: (*a*) maximum value of magnitude of lift coefficient C'_L versus the axial flow parameter; (*b*) lift coefficient C''_L versus dimensionless time. The solid lines are a best fit to the data. The computational runs corresponding to the different symbols are indicated in table 1.

U (Cases B.7–B.9) but the same values of the axial flow parameter and the vortex Reynolds number. The maximum lift coefficient magnitude decreases with increase in impact parameter, but the lift itself is found to increase nearly linearly with U. This observation implies that the ratio $C'_L \equiv L/\frac{1}{2}\rho\Gamma U\sigma_0$ should depend only on the axial flow parameter $A \equiv 2\pi\sigma_0 w_0/\Gamma$. The maximum value of $|C'_L|$ is plotted versus A in figure 22(*a*) for Cases B.1–B.10 and is found to exhibit an approximately linear dependence. Assuming that C'_L varies linearly with A, we correlate all of our data (Cases B.1–B.10) by plotting a new lift coefficient $C''_L \equiv L/\pi\rho U w_0\sigma_0^2$ versus the dimensionless time in figure 22(*b*). The root-mean-square variation of the maximum lift coefficient from the best-fit curve in figure 22(*b*) is 14%.

5. Conclusions

Computations are reported for cutting of an initially columnar vortex by a blade for cases both with and without axial vortex flow and for different values of the vortex Reynolds number, impact parameter and thickness parameter. The computations are validated by comparing to experimental data and to previous (inviscid) computational results. During blade penetration into the vortex core, cross-diffusion between vorticity in the blade boundary layer and that within the vortex causes vortex lines originating in the columnar vortex to reconnect to those within the blade boundary layer. It is found, however, that the vortex is always incompletely cut by the blade, such that a vortex sheet originating as a remnant of the columnar vortex will remain wrapped about the blade leading edge for a significant time following passage of the blade through the vortex core for all Reynolds numbers. This phenomenon is caused by a reversal in the direction of the vortex-induced spanwise velocity along the blade leading edge as the vortex centroid is advected past the leading edge. Once the spanwise velocity changes direction, the sign of the surface vorticity at the blade leading edge quickly changes to be the same as that of the columnar vortex, so that the remaining sections of the columnar vortex have no vorticity of the opposite sign with which to cross-diffuse (which in turn halts the vortex line reconnection process). The percentage of the vortex left in this remnant vortex sheet wrapping about the blade is not significantly affected by Reynolds number for the range of Reynolds numbers considered in the current work.

The presence of an axial flow within the columnar vortex causes development of asymmetry between the upper and lower blade surfaces. In agreement with previous experimental and computational studies, we find that the vortex core radius increases within the upper portion of the vortex (which is axially compressed by the axial flow) and decreases in the lower portion of the vortex (which is stretched by the axial flow). The decreased core radius in the lower section of the cut vortex results in an increased axial vorticity component and increased swirl velocity at the periphery of the vortex core. This increase in the swirl velocity leads to boundary-layer separation and ejection of fluid from the blade boundary layer just upstream of the section of the cut vortex below the blade. We examine the time variation of the axial flow and the positive circulation within the blade centreplane as the blade penetrates into the vortex core in order to determine the relationship between cutting of the vortex by reconnection of vortex lines and blockage of the axial flow. Somewhat surprisingly, it is found that the axial flow is blocked quickly enough during blade penetration into the vortex that no separation of boundary-layer fluid from the blade leading edge is observed as the blade penetrates close to the vortex centre, at least for the range of Reynolds numbers considered in the current study.

The asymmetry of the blade upper and lower surfaces in the presence of an axial flow leads to a transient lift force on the blade. The predicted peak value of the lift force compares reasonably well with experimental results. The lift force magnitude is found to increase monotonically with increase in axial velocity and impact parameter, but not to be significantly influenced by change in Reynolds number or blade thickness ratio in the range of values considered in the study. Comparison of computed results at low Reynolds number with experimental data at much higher Reynolds number indicates that the maximum lift force on the blade is approximately independent of Reynolds number, but that the time variation of the lift force is more rapid during blade penetration for higher Reynolds number cases. We also note that while the presence of some non-zero viscosity is necessary for vortex cutting to occur, most of the physical

processes described in the previous paragraphs which govern the cutting process are inviscid. Even such inherently viscous processes as vorticity cross-diffusion are not strongly influenced by viscosity, since the vorticity gradient at the blade leading edge will become increasingly steep as the blade penetrates into the vortex core. Similarly, boundary-layer ejection typically corresponds to the presence of a stagnation line in the inviscid flow field at the surface.

The observation that the blade lift increases approximately linearly with both blade–vortex impact velocity U and axial velocity w_0 leads to the development of a correlation for the blade lift coefficient, where the maximum lift coefficient is expressed as a function of density, core radius, impact velocity and vortex axial velocity. This correlation fits all data obtained in the study with a root-mean-square variation of the maximum lift coefficient of 14%. It is of interest that much of the focus in the rotorcraft aerodynamics community is on accurate prediction of circulation of rotor wake vortices; however, the present study suggests that accurate prediction of the vortex core radius and axial velocity is significantly more important for this type of blade–vortex interaction.

Research support for this project was provided by Hitachi Industries, Ltd. Dr T. Okamura and Mr T. Nagahara are the contract monitors. The encouragement and support of Professor V. C. Patel and Dr Yong Lai for this research is gratefully acknowledged. We also acknowledge prior support for research on a related topic from the US Army Research Office (grant number DAAH04-96-1-0081, Dr T. L. Doligalski program manager).

REFERENCES

Ahmadi, A. R. 1986 An experimental investigation of blade-vortex interaction at normal incidence. *AIAA J. Aircraft* **23**, 47–55.

Cary, C. M. 1987 An experimental investigation of the chopping of helicopter main rotor tip vortices by the tail rotor. *NASA CR*-177457.

Doolan, C. J., Coton, F. N. & Galbraith, R. A. McD. 2001 Surface pressure measurements of the orthogonal vortex interaction. *AIAA J.* **38**, 88–95.

Green, R. B., Doolan, C. J. & Cannon, R. M. 2000 Measurements of the orthogonal blade-vortex interaction using a particle image velocimetry technique. *Exps. Fluids* **29**, 369–379.

Issa, R. 1985 Solution of the implicit discretized fluid flow equations by operator splitting. *J. Comput. Phys.* **62**, 40–65.

Johnston, R. T. & Sullivan, J. P. 1992 Unsteady wing surface pressures in the wake of a propeller. *AIAA Paper* 92-0277.

Kida, S. & Takaoka, M. 1994 Vortex reconnection. *Annu. Rev. Fluid Mech.* **26**, 169–189.

Krishnamoorthy, S. & Marshall, J. S. 1994 An experimental investigation of 'vortex shocks'. *Phys. Fluids* **6**, 3737–3741.

Krishnamoorthy, S. & Marshall, J. S. 1998 Three-dimensional blade-vortex interaction in the strong-vortex regime. *Phys. Fluids* **10**, 2828–2845.

Lai, Y. G. 2000 Unstructured grid arbitrarily shaped element method for fluid flow simulation. *AIAA J.* **38**, 2246–2252.

Lee, J. A., Burggraf, O. R. & Conlisk, A. T. 1998 On the impulsive blocking of a vortex-jet. *J. Fluid Mech.* **369**, 301–331.

Leverton, J. W., Pollard, J. S. & Wills, C. R. 1977 Main rotor wake/tail rotor interaction. *Vertica* **1**, 213–221.

Marshall, J. S. 1994 Vortex cutting by a blade. Part I. General theory and a simple solution. *AIAA J.* **32**, 1145–1150.

Marshall, J. S. & Grant, J. R. 1996 Penetration of a blade into a vortex core: vorticity response and unsteady blade forces. *J. Fluid Mech.* **306**, 83–109.

Marshall, J. S. & Krishnamoorthy, S. 1997 On the instantaneous cutting of a columnar vortex with non-zero axial flow. *J. Fluid Mech.* **351**, 41–74.

Melander, M. V. & Hussain, F. 1989 Cross-linking of two anti-parallel vortex tubes. *Phys. Fluids* A **1**, 633–635.

Nagahara, T., Sato, T. & Okamura, T. 2001 Effect of the submerged vortex cavitation occurred in pump suction intake on hydraulic forces of mixed flow pump impeller. *CAV 2001: 4th Intl Symp. on Cavitation, Pasadena, California.* (ed. C. Brennen, S. Ceccio & R. Arndt).

Wang, T., Doolan, C. J., Coton, F. N. & Galbraith, R. A. M. 2002 Experimental study of the three-dimensionality of orthogonal blade-vortex interaction. *AIAA J.* **40**, 2037–2046.

Weigand, A. & Gharib, M. 1997 On the evolution of laminar vortex rings. *Exps. Fluids* **22**, 447–457.